


## Free-surface aeration in dam break waves: an experimental study

View metadata, citation and similar papers at [core.ac.uk](http://core.ac.uk)

brought to you by  CORE

provided by University of Queensland eSpace

**ABSTRACT:** New air–water flow experiments were conducted in the leading edge of dam break waves. The data highlighted the chaotic nature of the surge and provided new insights in the distributions of void fraction, velocity and air/water chord sizes. The results demonstrated a highly aerated surge front with a developing turbulent boundary layer. At the leading edge, observed mean air contents exceeded 40 to 50%, implying that sediment motion would be predominantly bed-load.

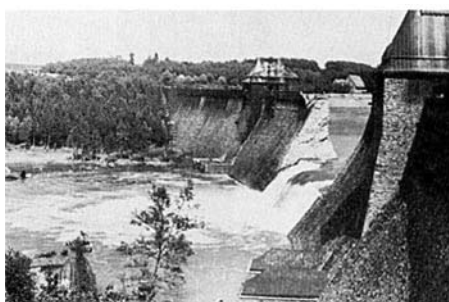
### 1 INTRODUCTION

Flood waves resulting from dam breaks have been responsible for numerous losses of life (Fig. 1). Related cases include flood waves resulting from gate malfunction or failure of an upstream reservoir, flash floods and debris flows. Other forms of sudden flood waves include natural lake breach, glacier lake outburst floods (GLOF) and flooding of valleys during armed conflicts (Fig. 1A). Despite few earlier studies (DRESSLER 1954, ESCANDE et al. 1961), current knowledge of dam break wave surging down rough sloping waterways is still rudimentary while the aerated nature of the advancing front, evidenced by photographs and witnesses, remains un-quantified. During a debris flow flash flood, local witnesses reported that “*the surge front advanced rather slowly down-valley as a huge ‘black’ mass of water full of debris. The surge emitted a loud noise ‘like many helicopters’ and a foul mud-smell. The valley bottom was wreathed in misty clouds of water vapour; the river banks were trembling; houses were shaking*” (GALAY 1987, p. 2.36).

During the present study, flash flood surges were generated in a large stepped chute. This investigation provides new information on the rate of energy dissipation and wave front propagation. Unsteady two-phase flow measurements were conducted in the surge front to gain new insights into the air–water flow and its possible impact on debris and sediment motion.

### 2 EXPERIMENTAL SETUP

New experiments were performed in the 25 m long 0.5 m wide flume ( $S_0 \approx 0.065$ ,  $\theta = 3.4^\circ$ ) previously used by CHANSON (2003) (Table 1). A precise discharge was delivered by a pump controlled



(A)



(B)

Figure 1. Photographs of dam break. (A) Möhne dam break (17 May 1943) (B) Zeyzoun dam break (4 June 2002).

Table 1. Summary of unsteady dam break wave flow experiments.

Experiment (1)	$\theta$ (deg.) (2)	h (m) (3)	Q(t=0+) (m <sup>3</sup> /s) (4)	Steady flow regime (5)	Remarks (6)
Brushes Clough dam	18.4	0.19	0.5	Skimming	Inclined downward steps, trapezoidal channel (2 m bottom width).
CHANSON (2003) Series 1	3.4	0.143	0.019 to 0.075	Nappe NA3	10 horizontal steps (l = 2.4 m). W = 0.5 m. Nozzle depth: d <sub>n</sub> = 0.030 m.
Series 2	3.4	0.0715	0.040 to 0.075	Trans./Skim.	18 horizontal steps (l = 1.2 m). W = 0.5 m. Nozzle depth: d <sub>n</sub> = 0.030 m.
Present study	3.4	0.0715	0.050 0.060 0.065 0.070	Skimming	18 horizontal steps (l = 1.2 m). W = 0.5 m. Nozzle depth: d <sub>n</sub> = 0.030 m. Air–water flow measurements on Step 16.

Notes: Q(t=0+): initial discharge; d<sub>n</sub>: approach flow depth; h: Step height; l: step length.

with an adjustable frequency AC motor drive Taian T-Verter K1/N1 (Pulse Width Modulated design), enabling an accurate discharge adjustment in a closed-circuit system. The flow was fed through a smooth convergent nozzle. The nozzle exit was 30 mm high and 0.5 m wide. The stepped invert configuration consisted of a 2.4 m long horizontal invert followed by 18 identical steps (h = 0.0715 m, l = 1.2 m).

## 2.1 Instrumentation

The flow rates in steady flow conditions were measured with a Dall™ tube flowmeter, calibrated on site with a sharp-crested weir. The accuracy on the discharge measurement was about 2%. The surging flow was studied with digital still- and video-cameras using high-shutter speed (1/1,000 to 1/10,000 sec.).

Air–water flow properties were measured with two systems. Air concentrations and bubble count rates were recorded with a series of single-tip conductivity probes (needle probe design). Each probe consisted of a sharpened rod (platinum wire  $\varnothing = 0.35$  mm) which was insulated except for its tip and set into a metal supporting tube (stainless steel surgical needle  $\varnothing = 1.42$  mm) acting as the second electrode. The second apparatus was a double-tip conductivity probe. The inner electrode was a platinum wire (99.9% purity,  $\varnothing = 0.15$  mm) and the outer electrode was a stainless steel surgical needle ( $\varnothing_{int} = 0.5$  mm,  $\varnothing_{ext} = 0.8$  mm). Each tip was identical and the distance between sensor was  $\Delta x_{tip} = 8.9$  mm. The probe was designed with a small frontal area of the first tip (i.e.  $0.5$  mm<sup>2</sup>) and with a displaced second tip (offset: 1.4 mm). The design prevents wake disturbance from the leading tip and tests showed the absence of wake during all experiments (CHANSON 1995). With both systems of probes, the probe sensors were aligned in the flow direction and excited by an air bubble detector developed at the University of Queensland (UQ82.518) with a response time of less than 10  $\mu$ s and calibrated with a square wave generator. The probe output signals were scanned at 10 kHz per channel for six seconds.

Data acquisition was triggered manually immediately prior to the flow arrival. Visual observations showed that the wave front was roughly two-dimensional. All measurements were taken on the centreline of step 16 at several distances  $x'$  from the step vertical face (Fig. 2). At each location  $x'$ , a single-tip conductivity probe (i.e. reference probe) was set on the invert, acting as a time reference, while the other probes were set at different elevations. Each experiment was repeated until sufficient data were obtained for each vertical profile. The displacement of the probes in the direction normal to the invert was controlled by a fine adjustment travelling mechanism. The error in the probe position was less than 0.2 mm and 2 mm in the vertical and horizontal directions respectively.

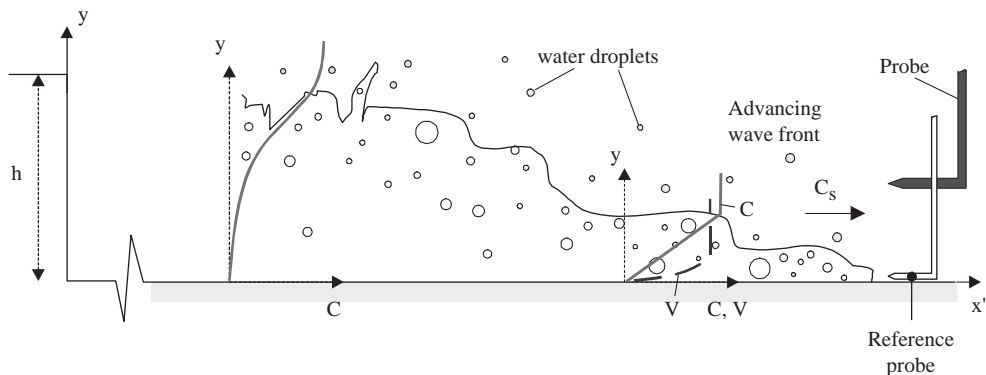


Figure 2. Definition sketch.

## 2.2 Data processing

Steps were painted with red and white stripes spaced 50 mm apart. Video-taped movies were analysed frame-by-frame. The error on the time was less than  $1/250$  s and the error on the longitudinal position of the wave front was  $\pm 1$  cm.

The conductivity probe signal outputs were processed using a single threshold technique. The threshold was set at about 50% of the air–water voltage range. Unsteady void fractions  $C$  and bubble count rates  $F$  were calculated during a short time interval  $\tau$  such as  $\tau = \Delta x / C_s$  where  $C_s$  is the surge front celerity measured with the video-cameras and  $\Delta x$  is the control volume streamwise length. Preliminary tests indicated that  $\Delta x \geq 70$  mm to contain a minimum of 5 to 20 bubbles (CHANSON 2003). The selection was consistent with the processing technique of STUTZ and REBOUD (2000). The bubble count rate was calculated as:  $F = N_{ab} / \tau$  where  $N_{ab}$  is the number of bubbles detected during the time interval  $\tau$ . Bubble and water chord sizes were deduced from measured chord times where the bubble chord time  $t_{ch}$  is defined as the time spent by the bubble on the probe tip.

Velocity data were calculated from individual droplet events impacting successively the two probe sensors. The velocity was deduced from the time lag for air-to-water interface detections between leading and trailing tips respectively. For each meaningful event, the interfacial velocity was calculated as:  $V = \Delta x_{tip} / \delta t$  where  $\Delta x_{tip}$  is the distance between probe sensors and  $\delta t$  is the interface traveling time between probe sensors.

## 2.3 Boundary flow conditions

Prior to the start of each experiment, the recirculation pipe system and convergent intake were emptied. The channel was initially dry. The pump was rapidly started. The electronic controller had a 5 sec. ramp. The pump reached its nominal power (i.e. discharge) at least 10 sec. prior to the water entering the channel. The flow rate  $Q(t = 0+)$  was maintained constant until at least 10 sec. after the wave front reached the downstream end of the flume (Table 1).

Previously, steady flow experiments were conducted in the same channel with smooth and stepped invert configurations (CHANSON and TOOMBES 2002). These steady air–water flow results provided the limiting conditions of the present study of unsteady flows.

# 3 BASIC RESULTS

## 3.1 Wave front propagation

For all experiments, visual observations showed that the wave front propagated basically as a succession of free-falling nappe, nappe impact and horizontal runoff. For comparison, the flow regime observations in steady flows are summarised in Table 1 (column 5). The surging flow exhibited a nappe flow behaviour for all discharges and geometries (Table 1). The wave front was chaotic and highly aerated, in particular for the largest flow rates, with strong spray, splashing and

wavelets. Water packets were commonly projected to heights greater than 3 to 4 step heights, while some droplets reached heights of more than 8 to 10 step heights. Visually the experiments in the large-size flume had a similar appearance to the surging flow observed at Brushes Clough dam spillway (Table 1).

The propagation of the wave leading edge was recorded for a range of unsteady flow conditions (Table 1). Although experimental observations suggested an almost linear relationship between wave front location and time, wave front celerity data showed that the flow was accelerated in the first 4 to 6 steps. Further downstream, a gradual decay in celerity was observed. The data were compared successfully with HUNT's (1982) theory for dam break wave down sloping chutes assuming an equivalent Darcy-Weisbach friction factor  $f = 0.05$ , irrespective of the discharge and step height. This flow resistance value is close to air-water flow measurement results in steady flow conditions yielding  $f \sim 0.047$  (CHANSON and TOOMBES 2002).

In the following sections, air-water flow properties, in the horizontal runoff flow region predominantly, are detailed.

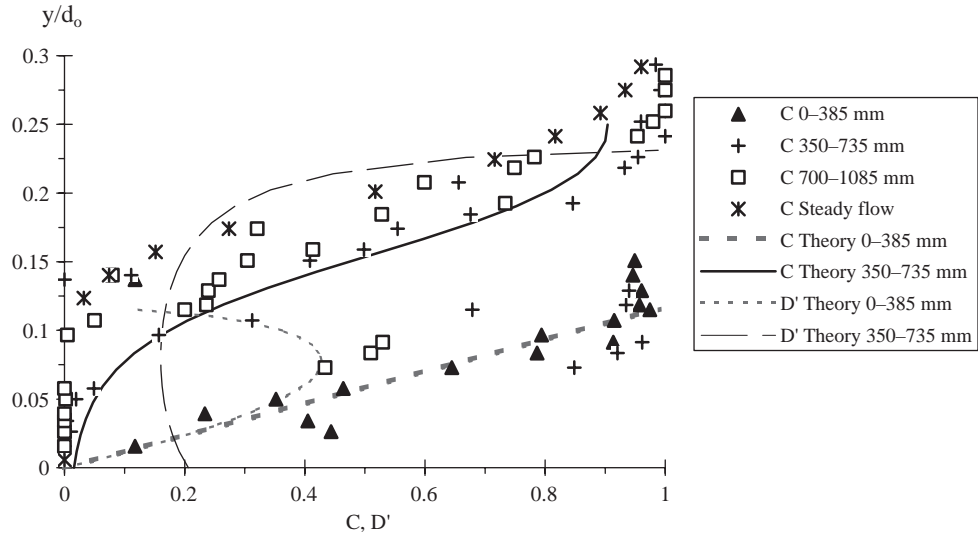
### 3.2 Void fraction distributions

Typical distributions of void fractions in the horizontal runoff are presented in Figure 3 at a location  $x'$ . Each void fraction data set was recorded at a time  $t$  measured from the first water detection by the reference probe, and time values are reported in figure caption. In Figure 3,  $y$  is the distance normal to the invert (Fig. 1),  $d_0$  is a measure of the initial discharge  $Q(t = 0+)$ :

$$d_0 = \frac{9}{4} * \sqrt[3]{\frac{Q(t = 0+)^2}{g * W^2}} \quad (1)$$

and  $W$  is the chute width. At the front of the wave, the void fraction distributions had a roughly linear shape:

$$C = 0.9 * \frac{y}{Y_{90}} \quad 0.1 < t * \sqrt{g/d_0} < 1.3 \quad (2)$$



	0-385 mm	350-735 mm	700-1085 mm
$t$ (s) =	0.079	0.223	0.367
$C_{mean}$ =	0.46	0.35	0.30

Figure 3. Dimensionless distributions of instantaneous void fractions  $C$  and air bubble diffusivity  $D'$  – Comparison with Equations (2) and (3) ( $Q(t = 0+) = 0.075 \text{ m}^3/\text{s}$ , step 16,  $x' = 0.8 \text{ m}$ ,  $\Delta x = 385 \text{ mm}$ ).

where  $Y_{90}$  is the height where  $C = 0.90$ . For larger times  $t$ , the distributions of air concentration were best described by the diffusion model:

$$C = 1 - \tan h^2 \left( K' - \frac{y}{2 * D_o} + \frac{\left( \frac{y}{Y_{90}} - \frac{1}{3} \right)^3}{3 * D_o} \right) \quad t * \sqrt{g/d_o} > 1.3 \quad (3)$$

where  $K'$  and  $D_o$  are functions of the mean air content only (CHANSON 2003). Equations (2) and (3) are plotted for unsteady and steady flow conditions in Figure 3. The analytical models compare favourably with the data.

Equations (2) and (3) are analytical solutions of the advective diffusion of air bubbles assuming respectively the following distributions of dimensionless turbulent diffusivity of air bubbles:

$$D' = \frac{C * \sqrt{1-C}}{0.9} \quad 0.1 < t * \sqrt{g/d_o} < 1.3 \quad (4)$$

$$D' = \frac{D_o}{1 - 2 * \left( \frac{y}{Y_{90}} - \frac{1}{3} \right)^2} \quad t * \sqrt{g/d_o} > 1.3 \quad (5)$$

where  $D' = D_t / ((u_r)_{Hyd} * \cos \theta * Y_{90})$ ,  $D_t$  is the turbulent diffusivity,  $(u_r)_{Hyd}$  is the rise velocity in hydrostatic pressure gradient. Equations (4) and (5) are plotted in Figure 3 in thin dashed lines. The shape of Equation (4) is similar to the sediment diffusivity distribution developed by ROUSE (1937) which yields to the Rouse distribution of suspended matter.

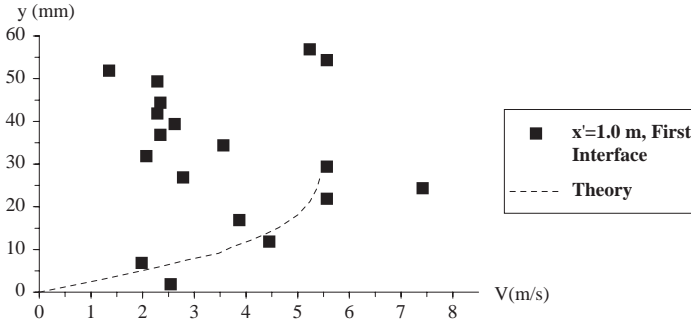
### 3.3 Discussion

The data demonstrated consistently strong aeration of the surge front, especially within the first 0.3 to 0.7 m behind the leading edge. The result has direct implications in terms of sediment processes at the front of flash floods and swash zone runoff on beaches. The large amount of “white waters” reduces buoyancy and increases the relative density of sediment particles. For example, the relative density  $s$  of quartz particles increases from 2.65 to 5.3 when the mean void fraction  $C_{mean}$  increases from 0 to 50%. The present findings imply that heavy sediment particles are more likely to be subjected to bed-load motion rather than suspension in flash flood surges.

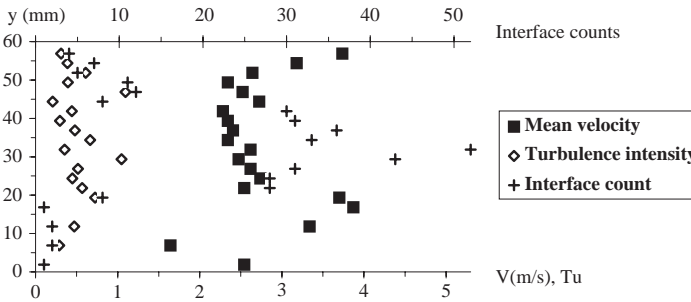
The data highlighted further a major change in void fraction distribution shape for  $t * \sqrt{g/d_o} \sim 1.2$  to 1.5. Possible explanations might include (a) a non-hydrostatic pressure field in the leading front of the wave, (b) some change in air–water flow structure between the leading edge and the main flow associated with a change in rheological fluid properties, (c) a gas-liquid flow regime change with some plug/slug flow at the leading edge and a homogenous bubbly flow region behind, and (d) a change in boundary friction between the leading edge and the main flow behind. All these mechanisms would be consistent with high-shutter speed movies of leading edge highlighting very dynamic spray and splashing processes.

## 4 VELOCITY DISTRIBUTIONS

Figure 4 presents interfacial velocity distributions in the horizontal runoff region. In Figure 4A, each data point represents the velocity of the first air-to-water interface detected at each location  $y$ . (The data were measured for  $t < 0.12$  s.) Figure 4B shows the mean velocity for an entire recording (i.e. for less than 6 sec.) at each location  $y$ . Each data point is the median velocity (or the average velocity if less than ten successful detections occurred). The number of successful interface detections is also shown for each location as well as the ratio of velocity standard deviation to mean velocity. For large interface counts, this ratio equals the turbulence intensity  $Tu$ . For small successive interface events ( $< 10$ ), the results are not statistically meaningful. Indeed Figure 4B highlights high levels



(A) Interfacial velocity of the first air-to-water interface – Comparison with Equation (6)



(B) Median interfacial velocity, turbulence intensity and number of successful interface detections (over about 5 sec.)

Figure 4. Velocity distributions at the surge leading edge ( $Q(t= 0+) = 0.065 \text{ m}^3/\text{s}$ , step 16,  $x' = 1.0 \text{ m}$ ).

of turbulence in the surging flow, with  $Tu$  ranging from 0.2 to 1.1 with a mean value of about 50% in Figure 4B.

In the horizontal runoff flow and at the surge leading edge, the data highlighted an unsteady boundary layer next to the invert with a potential flow region above (Fig. 4A). The finding is consistent with earlier laboratory experiments by MANO (1994) who studied unsteady wave runup using bubble tracer and high speed video. In Figure 4A, present data are compared with an analytical solution of the Navier-Stokes equations (first Stokes problem):

$$\frac{V}{U} = \text{erf}\left(\frac{y}{2 * \sqrt{\nu_T * t}}\right) \quad (6)$$

where  $U$  is a free-stream velocity,  $t$  is the time,  $\nu_T$  is the momentum exchange coefficient (or “eddy viscosity”) and  $\text{erf}$  is the Gaussian error function defined as:

$$\text{erf}(u) = \frac{2}{\sqrt{\pi}} * \int_0^u \exp(-t^2) * dt \quad (7)$$

Equation (6) is shown in Figure 4. The values of  $U$  and  $\nu_T$  were determined from the best fit of the data. For the data shown in Figure 4A,  $\nu_T = 1$  to  $2.3 \text{ E-}3 \text{ m}^2/\text{s}$ . Despite crude approximations leading to Equation (6), experimental results implied a turbulent boundary layer. For comparison, in laboratory wave runup and small debris flows, the boundary layer is believed to be laminar (MANO 1994, HUNT 1994), while the boundary layer is turbulent in prototype dam break flows and large debris flows (HUNT 1984, 1994).

Based upon void fraction and velocity measurements, the air bubble diffusivity  $D_t$  and eddy viscosity  $\nu_T$  which satisfy Equations (2) and (6) respectively yield a ratio  $D_t/\nu_T$  of about unity. The ratio  $D_t/\nu_T$  compares the effects of the difference in diffusion of a discrete particle and small

coherent fluid structure, as well as the effect of entrained air on the turbulence field. The result ( $D_t/\nu_T \propto 1$ ) seems to suggest strong interactions between the air bubble diffusion and momentum exchange processes.

## 5 AIR–WATER FLOW STRUCTURE

Air and water chord size measurements demonstrated a broad range of bubble and droplet sizes from less than 0.5 mm to more than 50 mm. The median air chord sizes were typically between 1 and 10 mm, and the distributions were skewed with a preponderance of smaller bubbles compared to the mean. Time variations in air–water flow structure were conducted at several cross-sections in the horizontal runoff flow (i.e.  $x' \geq 0.4$  m). At the wave leading edge ( $t < 0.1$  s), air and water chord sizes were comparable with median sizes of about 3–6 mm. This might suggest that individual bubble entrainment was associated with the ejection of water droplet of similar size. For larger times  $t$ , the order of magnitude of median air chord sizes remained basically constant and independent of time. But water chord sizes tended to increase with time, especially for  $y/Y_{90} < 0.7$ .

Such a different behaviour might be related to fundamental differences between air bubbles and water droplets. Water droplets have a momentum response time about 46,000 times larger than that of an air bubble of identical diameter (e.g. CROWE et al. 1998). As the bubble response time is significantly smaller than the characteristic time of the flow, bubble trapping in large-scale turbulent structures is a dominant mechanism in the bubbly flow region. Bubbles may remain trapped for very long times, the bubbly flow structure has some memory of its past, and it is affected by its previous structure. In the spray region, drop formation results from surface distortion, tip-streaming of ligaments and interactions between eddies and free-surface. Once ejected, the droplet response time is nearly two orders of magnitude larger the air flow response time. Most droplets have a short life and the spray region has little memory of its past. The spray structure may then change very rapidly in response to changes in flow conditions, while the bubbly flow region is deeply affected by its earlier structure.

## 6 SUMMARY AND CONCLUSIONS

New dam break wave experiments were conducted systematically down a 25 m long flat waterway with a stepped invert. Visual observations highlighted the chaotic nature of the advancing flow associated with strong aeration of the leading edge. Unsteady air–water flow measurements were performed in the wave front using a series of conductivity probes. The results demonstrated quantitatively strong aeration of the leading edge and the presence of a turbulent boundary layer next to the invert. The results suggest predominantly bed-load sediment motion near the leading edge, because the sediment relative density is inversely proportional to the air and water fluid density.

Measurements of air and water chord sizes highlighted a wide range of bubble and droplet sizes. Time-variations of air–water flow structure were observed. At the leading edge entrained bubbles and ejected droplets had similar sizes. Behind, however, the median water chord sizes increased with time, although the bubble sizes did not change. Overall the results emphasised the complicated nature of the dam break wave flow and its leading edge.

## ACKNOWLEDGMENTS

The writer thanks his students Chung-hwee “Jerry” LIM, York-wee TAN, Chye-guan SIM, and Chee-chong TAN for their help and assistance.

## REFERENCES

CHANSON, H. (1995). “Air Bubble Entrainment in Free-surface Turbulent Flows. Experimental Investigations.” *Report CH46/95*, Dept. of Civil Engineering, University of Queensland, Australia, June, 368 pages.

- CHANSON, H. (2003). "Sudden Flood Release down a Stepped Cascade. Unsteady Air–Water Flow Measurements. Applications to Wave Run-up, Flash Flood and Dam Break Wave." *Report CH51/03*, Dept. of Civil Eng., Univ. of Queensland, Brisbane, Australia, 142 pages.
- CHANSON, H., and TOOMBES, L. (2002). "Energy Dissipation and Air Entrainment in a Stepped Storm Waterway: an Experimental Study." *Jl of Irrigation and Drainage Engrg.*, ASCE, Vol. 128, No. 5, pp. 305–315.
- CROWE, C., SOMMERFIELD, M., and TSUJI, Y. (1998). "Multiphase Flows with Droplets and Particles." *CRC Press*, Boca Raton, USA, 471 pages.
- DRESSLER, R. (1954). "Comparison of Theories and Experiments for the Hydraulic Dam-Break Wave." *Proc. Intl Assoc. of Scientific Hydrology Assemblée Générale*, Rome, Italy, Vol. 3, No. 38, pp. 319–328.
- ESCANDE, L., NOUGARO, J., CASTEX, L., and BARTHET, H. (1961). "Influence de Quelques Paramètres sur une Onde de Crue Subite à l'Aval d'un Barrage." *Jl La Houille Blanche*, No. 5, pp. 565–575.
- GALAY, V. (1987). "Erosion and Sedimentation in the Nepal Himalaya. An Assessment of River Processes." *CIDA, ICIMOD, IDRC & Kefford Press*, Singapore.
- HUNT, B. (1982). "Asymptotic Solution for Dam-Break Problems." *Jl of Hyd. Div.*, ASCE, Vol. 108, No. HY1, pp. 115–126.
- HUNT, B. (1984). "Perturbation Solution for Dam Break Floods." *Jl of Hyd. Engrg.*, ASCE, Vol. 110, No. 8, pp. 1058–1071.
- HUNT, B. (1994). "Newtonian Fluid Mechanics Treatment of Debris Flows and Avalanches." *Jl of Hyd. Engrg.*, ASCE, Vol. 120, No. 12, pp. 1350–1363.
- MANO, A. (1994). "Boundary Layer Developed near Surging Front." *Coastal Engineering in Japan*, Vol. 37, No. 1, pp. 23–39.
- ROUSE, H. (1937). "Modern Conceptions of the Mechanics of Turbulence." *Transactions*, ASCE, Vol. 102, pp. 463–543.
- STUTZ, B., and REBOUD, J.L. (2000). "Measurements within Unsteady Cavitation." *Experiments in Fluids*, Vol. 29, pp. 545–552.